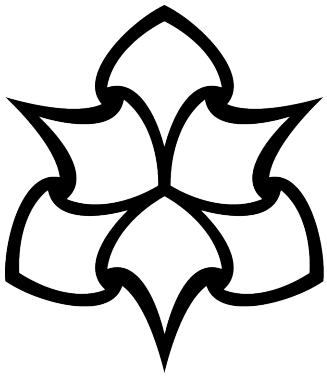

Manchester Metropolitan University

Gao, Jinqiang, Tian, Ye, Ni, Lianshan, Wang, Baowei, Zou, Kangyu, Yang, Yingchang, Wang, Ying, Banks, Craig E ORCID logoORCID: https://orcid.org/0000-0002-0756-9764, Zhang, Dou, Zhou, Kechao, Liu, Huan, Deng, Wentao, Zou, Guoqiang, Hou, Hongshuai and Ji, Xiaobo (2022) Robust cross-linked Na3V2(PO4)2F3 full sodium-ion batteries. Energy and Environmental Materials. e12485-e12485. ISSN 2575-0348

Downloaded from: https://e-space.mmu.ac.uk/632210/

Version: Published Version

Publisher: Wiley

DOI: https://doi.org/10.1002/eem2.12485

Usage rights: Creative Commons: Attribution 4.0

Please cite the published version

https://e-space.mmu.ac.uk

Check for updates

RESEARCH ARTICLE

Energy & Environmental Materials WILEY

Sodium-ion Batteries

Robust Cross-Linked $Na_3V_2(PO_4)_2F_3$ Full Sodium-Ion Batteries

Jinqiang Gao, Ye Tian, Lianshan Ni, Baowei Wang, Kangyu Zou, Yingchang Yang, Ying Wang, Craig E. Banks, Dou Zhang, Kechao Zhou, Huan Liu, Wentao Deng, Guoqiang Zou, Hongshuai Hou, and Xiaobo Ji*

Sodium-ion batteries (SIBs) have rapidly risen to the forefront of energy storage systems as a promising supplementary for Lithium-ion batteries (LIBs). $Na_3V_2(PO_4)_2F_3$ (NVPF) as a common cathode of SIBs, features the merits of high operating voltage, small volume change and favorable specific energy density. However, it suffers from poor cycling stability and rate performance induced by its low intrinsic conductivity. Herein, we propose an ingenious strategy targeting superior SIBs through cross-linked NVPF with multi-dimensional nanocarbon frameworks composed of amorphous carbon and carbon nanotubes (NVPF@C@CNTs). This rational design ensures favorable particle size for shortened sodium ion transmission pathway as well as improved electronic transfer network, thus leading to enhanced charge transfer kinetics and superior cycling stability. Benefited from this unique structure, significantly improved electrochemical properties are obtained, including high specific capacity (126.9 mAh g^{-1} at 1 C, 1 C = 128 mA g^{-1}) and remarkably improved long-term cycling stability with 93.9% capacity retention after 1000 cycles at 20 C. The energy density of 286.8 Wh kg^{-1} can be reached for full cells with hard carbon as anode (NVPF@C@CNTs//HC). Additionally, the electrochemical performance of the full cell at high temperature is also investigated (95.3 mAh g^{-1} after 100 cycles at 1 C at 50 °C). Such nanoscale dual-carbon networks engineering and thorough discussion of ion diffusion kinetics might make contributions to accelerating the process of phosphate cathodes in SIBs for large-scale energy storages.

1. Introduction

With the ever-growing attention to the utilization of large-scale renewable energy storage systems and devices, Li-ion batteries (LIBs) gradually play a dominant role in energy market, and is getting mature by the day. Nonetheless, with respect to the increasing cost of lithium resulted from its uneven distribution and limited resource in earth's crust, the growth and expansion of LIBs industry might be seriously restrained in the future.[1] Due to the more acceptable cost and wide distribution of sodium resources, as well as the referential experience from LIBs area, SIBs are becoming one of the most prospective alternatives for state-of-the-art LIBs.[2] However, the electrochemical performances of SIBs are far from satisfactory. Therefore, plenty of researches have been devoted to design and improve advanced electrode materials especially the cathode materials over the past few decades, to achieve satisfying performances of SIBs, including high energy/power density alongside long cycling lifespan.[3,4] To date, cathode materials of SIBs can be mainly categorized into four groups, i.e., layered transition-metal oxides, polyanion-type compounds, Prussian blue analogues, and tunnel-structure metal oxides.[5,6] Among them, most layered transition metal oxides and tunnel-structure metal oxides depict unsatisfying cycling performances and poor air-stability because

Dr. J. Gao, Dr. Y. Tian, Dr. L. Ni, B. Wang, Dr. K. Zou, Dr. W. Deng, Prof. G. Zou, Prof. H. Hou, Prof. X. Ji
College of Chemistry and Chemical Engineering, Central South University, Changsha 410083, China
E-mail: wentao_deng@csu.edu.cn
Prof. Y. Yang
College of Material and Chemical Engineering, Tongren University, Tongren 554300, China
Prof. Y. Wang
Department of Chemistry, The Chinese University of Hong Kong, Shatin, N. T., Hong Kong S.A.R., China
Prof. C. E. Banks
Faculty of Science and Engineering, Manchester Metropolitan University, Manchester UK
Prof. D. Zhang, Prof. K. Zhou
State Key Laboratory of Powder Metallurgy, Central South University, Changsha 410083, China
Dr. H. Liu
School of Materials Science and Engineering, Hunan Provincial Key Lab of Advanced Materials for New Energy Storage and Conversion, Hunan University of Science and Technology, Xiangtan 411201, China
Prof. X. Ji
School of Materials and Engineering, Zhengzhou University, Zhengzhou 450001, China
The ORCID identification number(s) for the author(s) of this article can be found under https://doi.org/10.1002/eem2.12485.

DOI: 10.1002/eem2.12485

© 2022 The Authors. *Energy & Environmental Materials* published by John Wiley & Sons Australia, Ltd on behalf of Zhengzhou University. This is an open access article under the terms of the Creative Commons Attribution License, which permits use, distribution and reproduction in any medium, provided the original work is properly cited.

of unstable structural transition and irreversible lattice oxygen loss during sodium ion insertion/extraction.[7,8] The practical application of Prussian blue analogues is hampered by CN^-. While polyanion-type compounds have many merits, including excellent cycling stability, sturdy crystalline and slight volume variations during the repeat charge/discharge processes.

Sodium vanadium-based fluorophosphate $Na_3V_2(PO_4)_2F_3$ (NVPF) is a typical polyanion-type compound with a sodium super ionic conductor (NASICON) structure, and due to its appealing electrochemical performances, it has shown high prospects in commercial application.[9–11] For instance, it can exhibit high average mid-working voltage (3.95 V vs Na^+/Na) with a theoretical specific capacity of approximately 128 mAh g^{-1}, and thus a theoretical energy density of ~507 Wh kg^{-1}.[12–14] However, this material experiences a major challenge of relatively poor intrinsic electronic conductivity (~10^{-12} S cm^{-1}) as a cathode, which gives rise to serious ohmic voltage drop, as well as critically hampered cycle life and high-rate capability. To address this problem, a range of strategies regarding material modification have been proposed, such as carbon matrix wrapping,[15] special transition metal element doping,[16] and morphology and nanocrystallization regulation,[17,18] etc.

Among these strategies above, coating NVPF with carbon-based materials is known as one of the most economic and effective ways. NVPF and carbon composite possess many merits: such as providing buffer for enhancing the electronic conductance, preventing NVPF from corrosion by the electrolyte, decreasing the cell polarization and repressing the volume changes during the intercalation/deintercalation processes.[19–21] For instance, researchers fabricated NVPF@C nanocomposite with a thin carbon shell through sol–gel method, and the composite exhibited a reversible specific capacity of 130 mAh g^{-1} at 0.5 C as well as capacity retention of 70% over 1000 cycles at 10 C.[22] In another work, $Na_3V_2(PO_4)_2F_3$ nanoparticles anchored on reduced graphene oxide (rGO) composite delivered high reversible capacity and outstanding high-rate performance.[23] If the carbon material is modified, the electrochemical performance of the composite can be further advanced. A nitrogen-doped carbon modified NVPF delivered a specific capacity of 94.5 mAh g^{-1} at 0.2 C, and 87% of the capacity was remined after 300 cycles at 30 C.[24] Apart from the capacity, the cycling performances of NVPF cathodes can be improved as well through carbon coating methods. However, satisfactory high-rate performance is hard to realize through single carbon layer as generally the electrical conductivity between particles can not be effectively enhanced under this circumstance. Therefore, to obtain advanced electrode with outstanding long-term cycling stability remains still a challenge. To address this problem, dual-carbon coating method via constructing three dimensional (3D) conductive network is an advantageous strategy, as the inter-particle and intra-particle charge transfer are both likely to be improved.[17]

In this work, NVPF caged in cross-linked dual-carbon frameworks is rationally designed and successfully fabricated, where NVPF is dispersed in robust carbonaceous matrix consisting of carbon layer and CNTs, as depicted in **Figure 1**. In the composite, the two carbonaceous materials function differently. The CNTs networks can provide boosted high-velocity interparticle electron conduction and excellent structural stability through constructing the chemical bridges between NVPF particles. Particularly, this carbon layer can effectively downsize NVPF particles, giving rise to shortened charge migration paths and enlarged contact area between the cathode and electrolyte, enhancing the structural stability to accommodate the rapid volume variations during repeated sodium ion extraction/insertion. As a consequence, the comprehensive electrochemical properties of NVPF@C@CNTs nanoparticles as SIBs cathode materials are improved remarkably, including good specific capacity (126.9 mAh g^{-1} at 1 C), impressive long-term durability (93.9% capacity reminded after 1000 cycles at 20 C) and exceptional energy density (405.5 Wh kg^{-1} based on the mass of cathode active materials). Besides, choosing an applicable fabrication method is of great importance to develop low-cost SIBs for large-scale energy storage systems. Our work employs specific heat treatment technique based on solid-state carbothermal reaction and this can realize the rapid preparation of NVPF@C@CNTs (1.1 kg) in the laboratory, suggesting the advantage in large-scale preparation.

2. Result and Discussion

2.1. Morphology and Physical Chemistry Properties

Starting with the structure description of NVPF, as shown in **Figure 2a**, the structural framework of NVPF is composed of $V_2O_8F_3$ bioctahedra and PO_4 tetrahedra, where the two units are connected through sharing O atoms along the ab-plane. This stable structure possesses plenty channels for fast sodium ion migration. There are two different positions for sodium ions in the framework, which are fully and partially occupied sites, respectively. In our previous work, the sodium ion migration mechanism and diffusion capability in NVPF were illustrated, and it is confirmed that sodium ions at the fully occupied sites is too stable to be extracted from the structure,[25,26] implying that the charge/discharge processes of NVPF are mainly dominated by the sodium ions

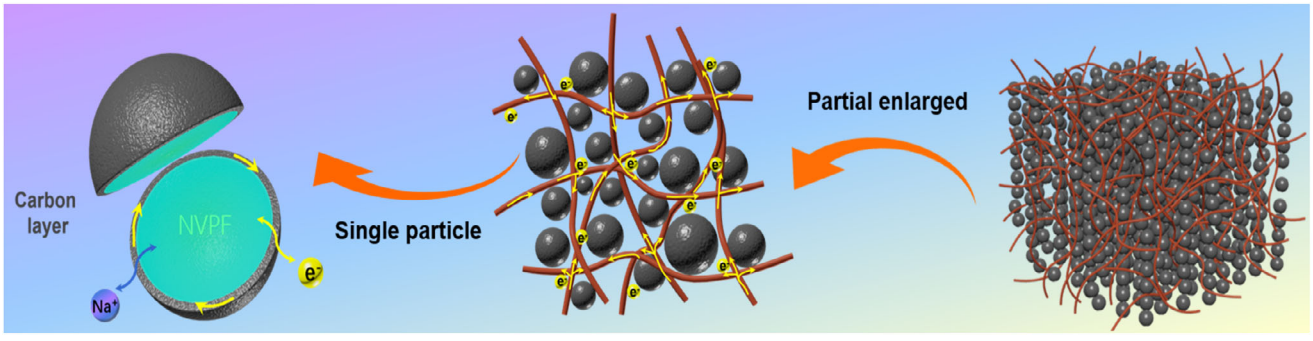

Figure 1. Illustration for the structure of NVPF@C@CNTs composites.

© 2022 The Authors. *Energy & Environmental Materials* published by John Wiley & Sons Australia, Ltd on behalf of Zhengzhou University.

25750356, 0, Downloaded from https://onlinelibrary.wiley.com/doi/10.1002/eem2.12485 by Manchester Metropolitan University, Wiley Online Library on [23/06/2023]. See the Terms and Conditions (https://onlinelibrary.wiley.com/terms-and-conditions) on Wiley Online Library for rules of use; OA articles are governed by the applicable Creative Commons License

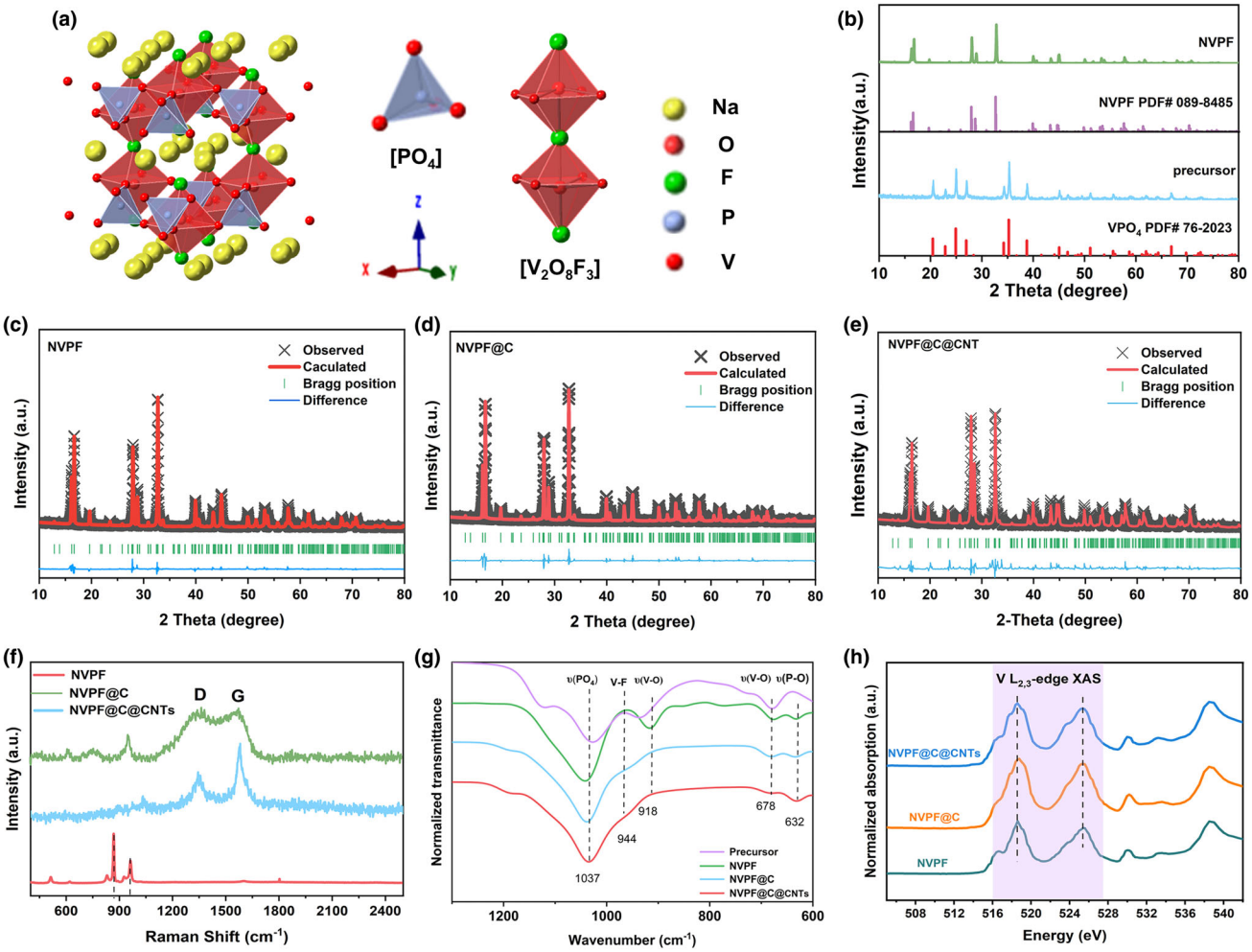

Figure 2. Structural characterizations of the prepared samples. a) Crystal structure of NVPF. b) XRD patterns of precursor and NVPF. c–e) Rietveld refined XRD patterns, f) Raman spectra curves, g) FT-IR spectra, and h) Normalized sXAS spectra of the V *L*-edge for NVPF, NVPF@C and NVPF@C@CNTs samples.

located at partially occupied sites. Its crystal structure was further clarified through XRD. As shown in Figure 2b, the peaks of precursor and as-prepared NVPF are in good agreement with VPO_4 (PDF# 76-20223) and NVPF (PDF# 089-8485), respectively. Figure S1a,b, Supporting Information, show the X-ray diffraction (XRD) patterns of as-prepared NVPF@C@CNTs under different annealing temperatures and calcining duration times. All the diffraction peaks are well-matched with the space group of $P4_2/mnm$ in NASICON structure except for the sample of NVPF@C@CNTs-550 °C. With the increase of annealing temperature, the degrees of crystallinity of NVPF are enhanced gradually. Impurity peaks can be observed in the sample annealed at 850 °C, which might be ascribed to the destruction of the NVPF crystal structure. As demonstrated in Figure S1b, Supporting Information, the particles are well crystallized after being annealed at 750 °C for 0.5 h. Noting that, in order to get satisfactory crystallinity, the condition 750 °C/2 h was selected to prepare electrode materials.

The Rietveld refinements (Fullprof software) of the as-prepared NVPF, NVPF@C and NVPF@C@CNTs powder samples (Figure 2c–e and Figure S1c, Supporting Information) are performed to obtain the lattice parameters (Tables S1 and S2, Supporting Information). It is noticed that the peak positions, intensity ratio, and peak sharpness of these XRD patterns are almost the same, indicating the high purity of all samples. For NVPF@C@CNTs, most of the diffraction peaks are consistent with the tetragonal NVPF phase, and the corresponding lattice parameters of space group $P4_2/mnm$ are a = b = 9.03 Å, c = 10.63 Å and V = 866.9 $Å^3$, which is in accordance with the NVPF standard crystal structure reported previously.[25] It demonstrates that the prepared material is well-crystallized. For the carbonaceous material in the composite, the characteristic peaks corresponding to CNTs (Figure S1d, Supporting Information) are not clearly detected in NVPF@C@CNTs, suggesting that either the peak intensities of CNTs are much lower than those of NVPF or the contents of CNTs are extremely low.

It is of great importance to figure out the carbon quantity in the composites, as it will affect the physiochemical properties of the NVPF based composites from many ways. To certify the existence and determine the quantity of the carbon, thermogravimetric analysis (TGA) was employed. The carbon amounts of bare NVPF, NVPF@C and NVPF@C@CNTs were evaluated to be <0.1 wt%, 5.9 wt%, and 4.1 wt%, respectively, based on the weight loss between 300 °C and 500 °C, as shown in Figure S2, Supporting Information. A small weight loss before 300 °C is due to the evaporation of surface-

© 2022 The Authors. *Energy & Environmental Materials* published by John Wiley & Sons Australia, Ltd on behalf of Zhengzhou University.

25750356, 0, Downloaded from https://onlinelibrary.wiley.com/doi/10.1002/eem2.12485 by Manchester Metropolitan University, Wiley Online Library on [23/06/2023]. See the Terms and Conditions (https://onlinelibrary.wiley.com/terms-and-conditions) on Wiley Online Library for rules of use; OA articles are governed by the applicable Creative Commons License

absorbed water, and the slight weight increase after 550 °C might be ascribed to the oxidation of trivalent vanadium in air. Note that the carbon is the overall weight of carbonaceous materials originated from CNTs and citric acid. With the existence of the carbon, it is not surprising that the tap density of NVPF@C@CNTs (1.039 g cm^{-3}) is lower than that of bare NVPF (1.147 g cm^{-3}) (Figure S3 and Table S3, Supporting Information). Additionally, the electronic conductivity of the composite has also been altered. Here, the electronic conductivities of all samples were investigated by using a four-probe meter (Table S4, Supporting Information). The electric conductivity of NVPF@C@CNTs (2.1×10^{-2} S m^{-1}) is much higher than those of NVPF (3.2×10^{-4} S m^{-1}) and NVPF@C (7.4×10^{-3} S m^{-1}). These results are attributed to the CNT networks with high conductivity and their decent electrical contacts with particles, which are beneficial for improving the electrochemical performances.

To further explore the detailed structure information of the obtained materials, they are characterized via Raman spectroscopy. As shown in the Raman spectra (Figure 2f and Figure S4, Supporting Information) of bare NVPF, the band at 937 and 1049 cm^{-1} are ascribed to the P–O symmetrical/asymmetrical stretching vibration of PO_4, respectively. As for NVPF@C and NVPF@C@CNTs, the two intense characteristic peaks at 1345 and 1585 cm^{-1} are assigned to disordered graphitic carbon from sp^3 carbon atoms (D-band) and crystalline graphitized carbon from sp^2 carbon atoms (G-band), respectively. Moreover, the calculated relative intensity ratios of D band to G band (I_D/I_G, defined to evaluate the structural disordering of carbon materials) of CNTs is about 0.38, and the ratio of NVPF@C@CNTs (about 0.76) is much smaller than that of NVPF@C (about 0.96). This suggests that the degree of graphitization of the dual-carbon networks is greatly enhanced due to the existence of CNTs, thus leading to superfast charge transmission as well as improved electrochemical properties.

The structure of all samples was also illustrated by Fourier transform infrared (FT-IR) spectroscopy, and the results were recorded in Figure 2g. The characteristic absorption peaks are quite distinct to tell. An absorption peak of PO_4^{3-} indexed to unsymmetrical stretching vibration is noticed at 1185 cm^{-1}, the broadband located at 1000–1150 cm^{-1} is ascribed to the asymmetric stretching vibration of P–O bonds in PO_4^{3-} tetrahedra, the bands at 682 and 632 cm^{-1} are ascribed to the symmetric stretching vibration and bending vibration of P–O, respectively. The band at 944 cm^{-1} demonstrates the presence of V–F bonds in $V_2O_8F_3$ bi-octahedral, while the band at 918 cm^{-1} is attributed to the stretching vibration of V–O bonds. Additionally, the absorbance of V–F bonds is particularly weaker than the other bonds, resulted from a small number of V–F in the lattice. Notably, the characteristic peak of V^{5+} in VO_6 octahedra at 760 cm^{-1} is not detected, which is attributed to the completely reduction of V^{5+} in V_2O_5.

X-ray photoelectron spectroscopy (XPS) tests and soft X-ray absorption spectroscopy (sXAS) measurements were performed to investigate the chemical states of V in the as-prepared samples. The main elemental signals (C 1s, O 1s, Na 1s, F 1s, P 2s, P 2p, and V 2p peaks) are observed in the survey XPS spectra (Figure S5a, Supporting Information). For the element V, a pair of peaks are detected from high-resolution spectra of V element (Figure S5b, Supporting Information), the sharp peak at the binding energy of ~517 eV is attribute to V $2p_{3/2}$ and the other less sharp peak at ~525 eV is ascribed to the electrons in V $2p_{1/2}$, both of which are characteristic peaks of V^{3+}.[28] In addition, the sXAS spectra of all the three samples further confirm +3 valence states for the V ions,[27] as shown in Figure 2h.

With the introduction of carbonaceous materials, the specific surface areas of the samples are increased slightly, as characterized by nitrogen adsorption–desorption technique (Figure S6, Supporting Information). According to the Brunauer–Emmett–Teller (BET) method, the specific surface areas of NVPF, NVPF@C and NVPF@C@CNTs are calculated to be 13.05, 16.73 and 18.93 m^2 g^{-1}, respectively. The increased specific surface area is beneficial for improving the contact between the cathode and electrolyte. The pore size in NVPF@C@CNTs is mainly distributed between 2–5 nm, as displayed by the Barrett–Joyner–Halenda (BJH) pore size distribution curve (the inset), and the mesoporous structure of NVPF@C@CNTs would facilitate the infiltration of electrolyte.

The morphology and microstructure of the samples were characterized by scanning electron microscopy (SEM) and transmission electron microscopy (TEM). It is found that carbonaceous materials can effectively alter the particle size of NVPF (**Figure 3**a–c, Figures S7 and S8, Supporting Information), and this carbon coating strategy have effectively fabricated a robust 3D cross-linked carbonaceous framework for electrochemical energy storage. The morphology of bare NVPF particles is the most regular among all the samples with an average particle size of 1–3 μm. The diameter of single nanoparticle in both NVPF@C and NVPF@C@CNTs are down to 100–500 nm, demonstrating that the growth of NVPF particles is significantly inhibited by the introduction of carbonaceous materials. Greatly, the electron and sodium ion diffusion are expected to be significantly improved, benefitted from the decreased particle size and the shortened diffusion path.

As shown in Figure S8a–f, NVPF nanoparticles are tightly wrapped by amorphous carbon layer (thickness about 10 nm) and evenly dispersed in the 3D network composed of connected CNTs. This unique 3D CNTs network can optimize the conductivity of NVPF composites and buffer the variation of stress during the sodium ions extraction/insertion. Furthermore, such intertwined CNT framework could effectively enhance the electron transport for long distances by forming the bridges between different NVPF particles, which is highly favorable for achieving superior rate performances of NVPF@C@CNTs. In the high-resolution TEM (HRTEM) images of samples (Figure 3d–f and Figure S8e), lattice fringes are clearly observed with the stripe spaces of 0.27, 0.23, 0.25 and 0.32 nm, which are assigned to the interplanar distance of (222), (223), (312), and (220) planes in tetragonal NVPF crystal, respectively. To confirm the element distribution and composition at the surface of NVP@C@CNTs, EDS mapping was conducted (Figure 3g). As depicted by the EDS elemental mapping images, Na, V, O, P, F, and C are distributed homogeneously in the composite, which is in good accordance with the full XPS survey spectra. It is found that the carbon element is densely and evenly distributed on the surface of NVPF (Figure S8, Supporting Information and Figure 3g), further confirming that NVPF is completely encapsulated by carbon layers. This uniform carbonaceous framework would facilitate sodium ions insertion/extraction with a fast speed, which is in favor of high-rate performances.

2.2. Electrochemical Performances of the Sodium-Ion Half Cell

In-situ XRD method was utilized to reveal the charge/discharge mechanism of NVPF@C@CNTs under the current density of 0.5 C and voltage range from 2.5 to 4.3 V. As presented in **Figure 4**a,b and Figure S9, Supporting Information, the diffraction peaks of (002), (220) and (222) crystal planes are located at 16.55°, 27.95° and

© 2022 The Authors. *Energy & Environmental Materials* published by John Wiley & Sons Australia, Ltd on behalf of Zhengzhou University.

25750356, 0, Downloaded from https://onlinelibrary.wiley.com/doi/10.1002/eem2.12485 by Manchester Metropolitan University, Wiley Online Library on [23/06/2023]. See the Terms and Conditions (https://onlinelibrary.wiley.com/terms-and-conditions) on Wiley Online Library for rules of use; OA articles are governed by the applicable Creative Commons License

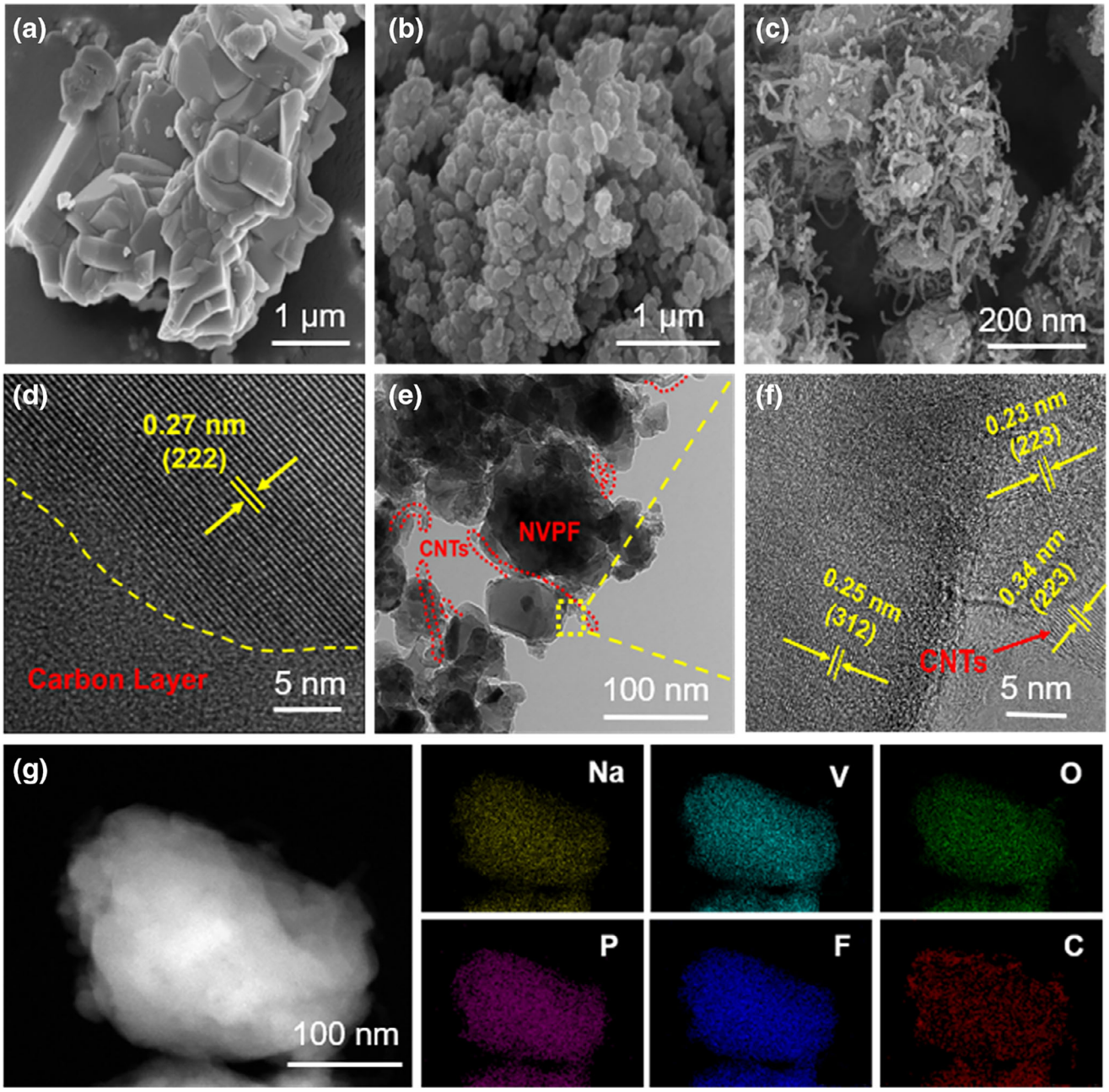

Figure 3. Morphology characterizations of samples. SEM images of a) NVPF, b) NVPF@C, and c) NVPF@C@CNTs. d–f) TEM and HRTEM images with different magnifications and g) elemental mapping images of NVPF@C@CNTs.

32.64° in the pattern of fresh electrode, respectively. When the NVPF@C@CNTs electrode is charged to 3.7 V, both (220) and (222) peaks are shifted to higher angles, while (002) peak is moved to lower angle. This is corresponding to the two-phase transformation from $Na_3V_2(PO_4)_2F_3$ to $Na_2V_2(PO_4)_2F_3$ with the extraction of sodium ion. As the voltage achieves 4.1 V, the positions of the three peaks are changed more obviously, indicating that sodium ion is extracted through the transformation from $Na_2V_2(PO_4)_2F_3$ to $NaV_2(PO_4)_2F_3$. A reverse angle changes are presented during the discharging process and all the diffraction peaks shift back to their initial positions as the NVPF@C@CNTs electrodes discharging to 2.5 V. These all prove that a single-phase solid solution reaction process appeared in both the charge and the discharge processes, and they also demonstrates that the electrochemical behavior of NVPF@C@CNTs electrodes is a rather reversible process of sodium ion extraction/insertion $[Na_3(V^{III})_2(PO_4)_2F_3 \rightleftharpoons Na(V^{IV})_2(PO_4)_2F_3 + 2Na^+ + 2e^-]$.

To explore the electrochemical properties of the samples, a series of coin-type half cells were assembled and carefully investigated through systematic electrochemical tests. The Cyclic voltammetry (CV) measurements of bare NVPF under 0.1 mV s^{-1} versus Na^+/Na were conducted (**Figure** 5a) to study the sodium ion insertion/extraction behavior. Two pairs of redox peaks, located respectively at 3.6/3.7 and 4.1/

© 2022 The Authors. *Energy & Environmental Materials* published by John Wiley & Sons Australia, Ltd on behalf of Zhengzhou University.

25750356, 0, Downloaded from https://onlinelibrary.wiley.com/doi/10.1002/eem2.12485 by Manchester Metropolitan University, Wiley Online Library on [23/06/2023]. See the Terms and Conditions (https://onlinelibrary.wiley.com/terms-and-conditions) on Wiley Online Library for rules of use; OA articles are governed by the applicable Creative Commons License

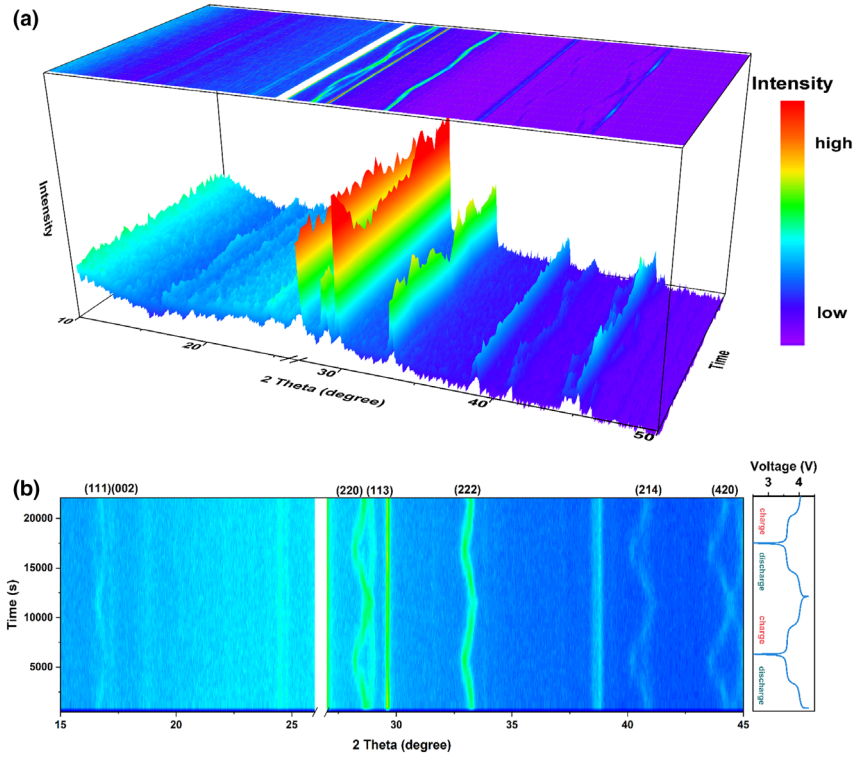

Figure 4. a) 3D in-situ XRD patterns and b) structural evolution of NVPF@C@CNTs electrodes during Na-intercalation/extraction under the applied current rate of 0.5 C between 2.5–4.3 V versus Na^+/Na.

4.2 V, are noticed in the curve, which are assigned to the V^{3+}/V^{4+} transform. The overlap of these redox peaks indicates the excellent reversibility over the successive cycling processes during the transformation between $Na_3V_2(PO_4)_2F_3$ and $NaV_2(PO_4)_2F_3$ as shown in the following.

$$Na_3(V^{III})_2(PO_4)_2F_3 \rightleftharpoons Na_2(V^{III}V^{IV})(PO_4)_2F_3 + Na^+ + e^-$$

$$Na_2(V^{III}V^{IV})(PO_4)_2F_3 \rightleftharpoons Na(V^{IV})_2(PO_4)_2F_3 + Na^+ + e^-$$

The galvanostatic charge–discharge (GCD) profiles of the first cycle of all samples at 1 C in the potential window of 2.0–4.3 V (vs Na^+/Na) are displayed in Figure 5b. Two pairs of flat and steady voltage plateaus (~3.7 and 4.1 V) can be observed, corresponding to the redox pair of V^{3+}/V^{4+} with two sodium extraction and insertion, which is well consistent with CV test results. More importantly, the specific capacity of NVPF@C@CNTs is greatly improved demonstrated by GCD test. Compared with bare NVPF (106.1 mAh g^{-1}) and NVPF@C (117.6 mAh g^{-1}), the designed NVPF@C@CNTs cathode delivers the highest initial discharge capacity of 126.9 mAh g^{-1} with the initial Coulombic efficiency (ICE) of 89.6%. The loss of charge capacity might be attributed to electrolyte decomposition and the formation of cathode electrolyte interphase (CEI). It is worth mentioning that the discharge capacity of NVPF@C@CNTs is close to its theoretical capacity, suggesting that the construction of dual-carbon conductive matrix would greatly enhance the electrochemical properties. In comparation with the other samples, NVPF@C@CNTs delivers the highest discharge capacity together with a corresponding capacity retention as high as 96.7% after 100 cycles at the rate of 1 C, as displayed in Figure 5c, implying the remarkably stable charge/discharge behavior. In addition, the improved electrochemical performances are still maintained even at high areal capacity (Figure S10, Supporting Information). Therefore, it is concluded that the introduced CNT is responsible for the high reversible specific capacity and remarkable cycling stability of NVPF@C@CNT composites. In addition, a comparison of the ICE and first-cycle capacity of the NVPF@C@CNTs electrodes in this work and that of previous work in the literatures are given in Table S5, Supporting Information. Our work has shown quite appealing and comparable first cycle capacity and ICE.

In order to investigate the electrochemical stability of different samples during cycling, the dQ/dV curves were recorded, respectively (Figure 5d–f). There are two pairs of characteristic peaks corresponding to the two voltage platforms in all curves, showing the consistence with the results of CV and GCD tests. However, different polarization performances are observed. As demonstrated in Figure 5d, bare NVPF suffers severe voltage degradation and undesirable discharge capacity loss. In contrast, polarization is significantly reduced due to the introduction of carbonaceous materials (Figure 5e,f), and the capacity contribution of high voltage platforms (~4.1 V) of NVPF@C@CNTs is increased remarkably, leading to desired energy density increase.

The effects of carbon framework on the rate performances were also measured at consecutive current densities varied from 1 to 20 C. As depicted in Figure 5g–i, NVPF@C@CNTs shows more favorable rate capability, mid-working discharge voltage, power density and energy density than other samples, and this is more distinctive at high current densities. The NVPF@C@CNTs electrode displays an average discharge capacity of 112, 110, 109, 107, 104, and 99 mAh g^{-1} at corresponding rates of 0.5, 1, 2, 5, 10, and 20 C, respectively. Surprisingly, when the current density returns to 0.5 C after 50 cycles, the discharge capacity recovers to 110 mAh g^{-1}, which is close to its initial capacity, exhibiting remarkable rate performances. This implies that the insertion/extraction of sodium ion in the NVPF@C@CNTs electrode is of excellent reversibility even at high rates. However, the rate performances of bare NVPF and NVPF@C are much inferior, suffering rapid capacity attenuation as the current density increases, indicating that the introduction of CNTs is beneficial to boost the electron transport and improve the sodium storage capability of NVPF accordingly.

As shown in Figure 5j, long-term cycling performances and Coulombic efficiencies of all samples at high current rate were conducted. The NVPF@C@CNTs shows marvelous long-term cycling stability at high rate of 20 C, and a specific capacity of 93.3 mAh g^{-1} is left even after 1000 cycles and a capacity retention of 93.9% is obtained (i.e., 0.0061% capacity loss per cycle). By contrast, the remaining specific capacities of bare NVPF and NVPF@C are only 52.1 and 65.9 mAh g^{-1} after 1000 cycles, corresponding to capacity retentions of 71.6% and 62.8%, respectively, which are much lower than that of

© 2022 The Authors. *Energy & Environmental Materials* published by John Wiley & Sons Australia, Ltd on behalf of Zhengzhou University.

25750356, 0, Downloaded from https://onlinelibrary.wiley.com/doi/10.1002/eem2.12485 by Manchester Metropolitan University, Wiley Online Library on [23/06/2023]. See the Terms and Conditions (https://onlinelibrary.wiley.com/terms-and-conditions) on Wiley Online Library for rules of use; OA articles are governed by the applicable Creative Commons License

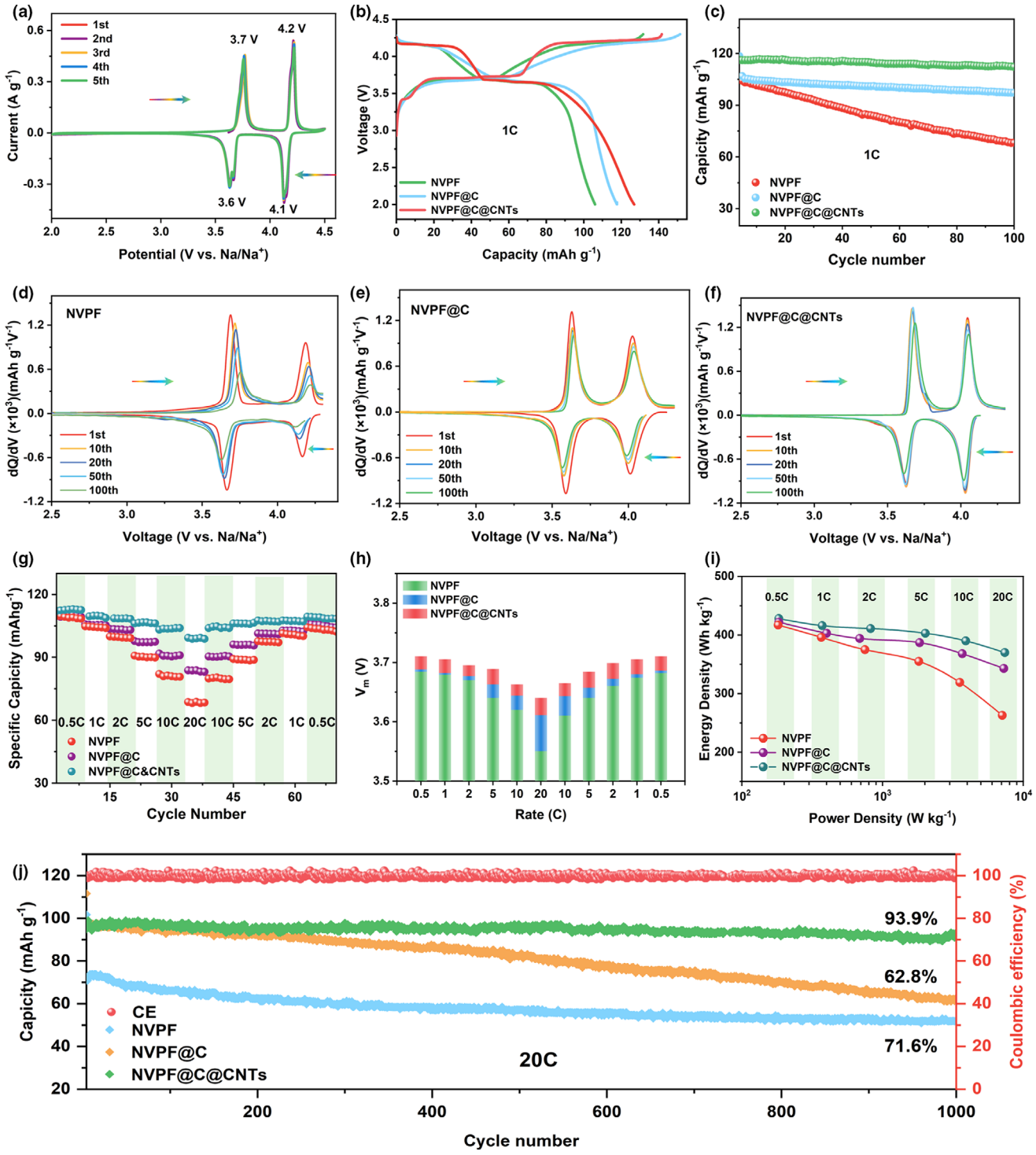

Figure 5. Electrochemical properties tested in coin-type half cells: a) CV curves for the first five cycles of bare NVPF at 0.1 mV s^{-1}. b) The GCD profiles of the first cycles at 1 C under the potential window of 2.0–4.3 V. c) Cycling performances at 1 C. d–f) The dQ/dV curves for the selected cycles at 1 C. g) Rate capability, h) corresponding mid-working discharge voltage at various current rates from 0.5 to 20 C, and i) Ragone plot at various rates. j) Long-term cycling performances and coulombic efficiency of all samples at 20 C rate for 1000 cycles in the voltage range of 2.5–4.3 V.

NVPF@C@CNTs. This significant difference of initial discharge capacity between bare NVPF and NVPF@C@CNTs should be ascribed to the powerful conductive network constructed with closely attached carbon layer and cross-linked CNTs. This unique conductive network can make the discharge process more sufficient than the other samples through accelerating the electron transport and shortening the sodium diffusion

© 2022 The Authors. *Energy & Environmental Materials* published by John Wiley & Sons Australia, Ltd on behalf of Zhengzhou University.

25750356, 0, Downloaded from https://onlinelibrary.wiley.com/doi/10.1002/eem2.12485 by Manchester Metropolitan University, Wiley Online Library on [23/06/2023]. See the Terms and Conditions (https://onlinelibrary.wiley.com/terms-and-conditions) on Wiley Online Library for rules of use; OA articles are governed by the applicable Creative Commons License

path, which is beneficial for delivering high discharge capacity. Besides, the carbon layer closely coated on the surface of particles prevents NVPF from corrosion by the electrolyte and represses the volume changes during the charge/discharge processes, enabling NVPF@C@CNTs marvelous long-term cycling performances even at high rate.

Moreover, as shown in Figure S11a, Supporting Information, the capacity retention of NVPF@C@CNTs is close to 50% after a ultralong-term cycling test over 10 000 cycles at 20 C. To get a better understanding of the superior structural stability, the XRD and SEM tests of NVPF@C@CNTs materials before and after cycling process were conducted. No obvious discrepancies can be found between pristine NVPF@C@CNTs and the cycled electrode (Figure S12, Supporting Information), which indicates that double carbon-wrapped NVPF@C@CNTs nanocomposite possesses brilliant structural stability in relieving internal pressure originated from electronic transport and sodium ion insertion/extraction. To investigate the reason for deteriorated electrochemical performances, the NVPF@C@CNTs electrode was reassembled with new metallic Na after 10 000 cycles. Surprisingly, the reassembled cell exhibits a discharge capacity as high as 100 mAh g^{-1} at the first cycle (Figure S11b, Supporting Information). This result demonstrates that the reason for the deterioration of the battery might be the consumption or decomposition of the electrolyte or the dendrite problem of the negative electrode, rather than the decay of the positive electrode material, which further confirms the robust structure of the NVPF@C@CNTs electrode material at high rates.

2.3. Electrochemical Sodium-Storage Behavior

The galvanostatic discharge profiles tested under the voltage range from 0.5 C to 20 C are exhibited in **Figure 6**a–c and Table S6, Supporting Information. It is found that the NVPF@C@CNTs cathode possesses the lowest potential polarization, which is closely associated with the most stable structure compared with the other electrodes, especially at the increased current rates. CV tests were utilized to further confirm the Na-migration kinetics in the samples. The electrodes were cycled in the voltage range of 2.0–4.5 V versus Na^+/Na with scan rates of 0.1, 0.2, 0.5, 1.0, 2.0, 3.0 and 5.0 mV s^{-1}. As depicted in Figure 6d–f, with

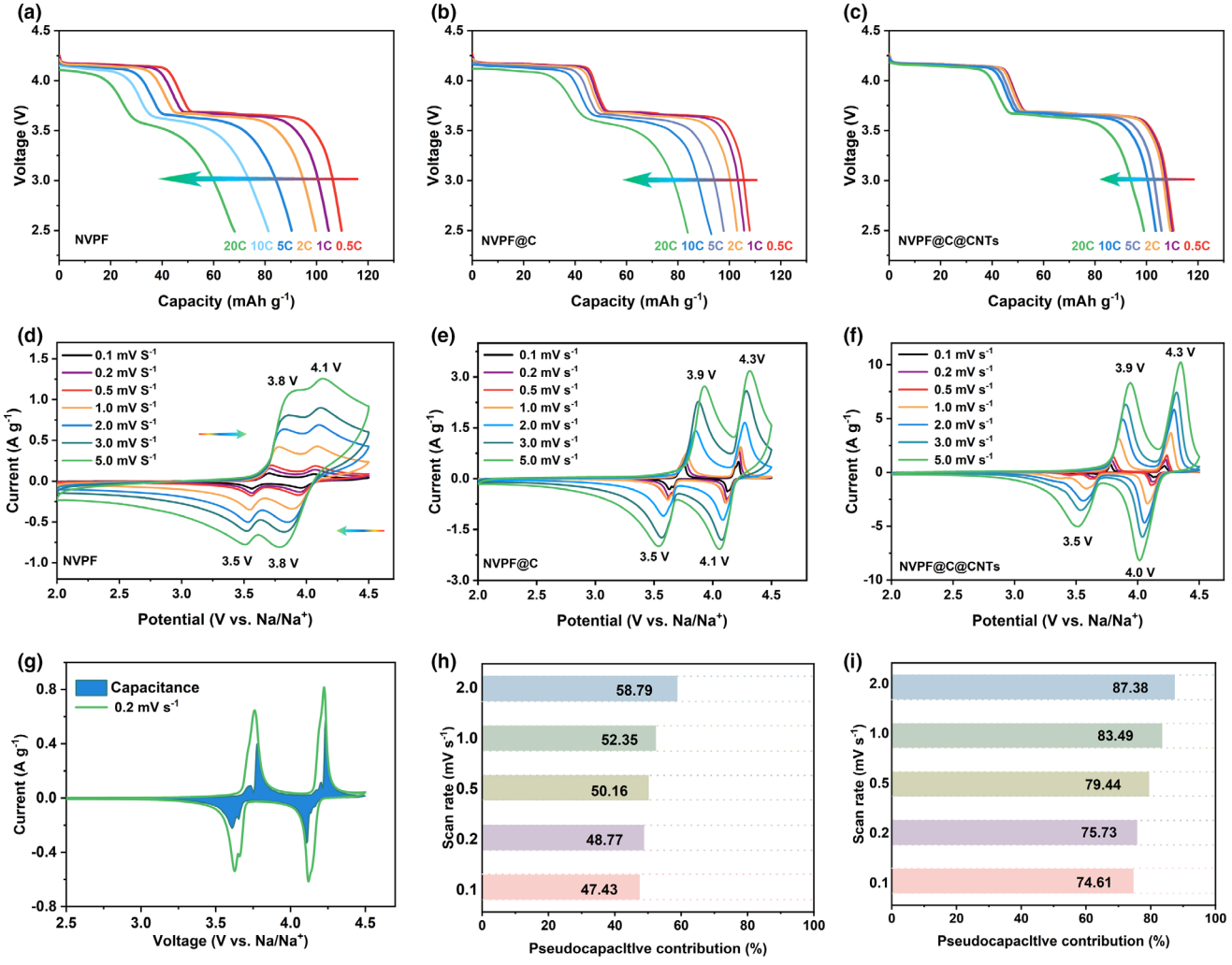

Figure 6. a–c) The discharge profiles at various current rates. d–f) CV curves at multiple scan rates ranging from 0.1 to 5 mV s^{-1}. g) CV curves and calculated pseudo-capacitance fraction (blue region) of bare NVPF at 0.2 mV s^{-1} (vs Na^+/Na). Contribution ratios of the capacitive-controlled capacity at different scan rates of h) NVPF and i) NVPF@C@CNTs.

© 2022 The Authors. *Energy & Environmental Materials* published by John Wiley & Sons Australia, Ltd on behalf of Zhengzhou University.

25750356, 0, Downloaded from https://onlinelibrary.wiley.com/doi/10.1002/eem2.12485 by Manchester Metropolitan University, Wiley Online Library on [23/06/2023]. See the Terms and Conditions (https://onlinelibrary.wiley.com/terms-and-conditions) on Wiley Online Library for rules of use; OA articles are governed by the applicable Creative Commons License

the increase of scanning rates, the current intensities, area of the CV curves and positions of redox peaks are changed, which is attributed to the increased polarization. Moreover, the linear relations between the logarithm of peak current and logarithm of scan rate are presented in Figure S13, Supporting Information. The b values for the peaks of all the samples are above 0.5, indicating the existence of pseudo-capacitance behavior. What calls for special attention is that the b values of NVPF@C@CNTs are close to 0.9, suggesting that the electrochemical reaction system is mainly controlled by capacitance. The total current contribution of pseudo-capacitance for bare NVPF is calculated to be 48.77% at scan rate of 0.2 mV s^{-1} (Figure 6g). Contributions of the capacitive-controlled capacity at selected scanning rates for NVPF cathode are much lower than those of NVPF@C@CNTs (Figure 6h,i). This proves that the electrochemical performances of NVPF@C@CNTs cathode at high rates has been effectively improved through downsizing the particle size and optimizing surface-interface of the electrode composites by this double carbon coating strategy.

The galvanostatic intermittent titration technique (GITT) measurements were conducted with an alternately charged time of 1200 s at 0.1 C, followed by a resting time of 7200 s, and single step of titration curves are presented in Figure S14, Supporting Information. The variation of all the calculated diffusion coefficients (D_{GITT}) under different states over the first charge and discharge process of NVPF-based electrodes are demonstrated in **Figure 7**a–c and Figure S15, Supporting Information. The values of D_{GITT} are all worked out to be in the range of 10^{-12}–10^{-8} cm^2 s^{-1}, showing a rapid diffusion capability of this NASICON-type structure. During charge/discharge processes, the values at low-potential plateaus (around 3.7 V) are obviously smaller than that at high-potential plateaus (about 4.1 V), agreeing well with the CV results. Additionally, the D_{GITT} of NVPF@C@CNTs cathode is the highest among all the samples, confirming the satisfactory ionic diffusion kinetics benefited from improved electronic conductivity and smaller particle size caused by 3D CNTs capping.

Electrochemical impedance spectroscopy (EIS) was employed to investigate the electrochemical properties and electrode reaction kinetics of different samples. The EIS tests were conducted in the frequency ranging from 10^5 to 0.01 Hz, and the Nyquist plots of the electrodes before and after cycling are illustrated in Figure 7d,e. Similar behaviors are observed for all the samples, including one semicircle and an inclined line. The insets shown in the figures are simplified equivalent circuit models to analyze the impedance spectra, where the Rs ohmic resistance is corresponded to electrolyte resistance, the Rct charge-transfer resistance is related to the diffusion of the sodium ion between the electrode and electrolyte, and the Zω Warburg impedance is assigned to sodium ion diffusion in the composites. Constant phase element (CPE) is associate with the double layer capacitance and

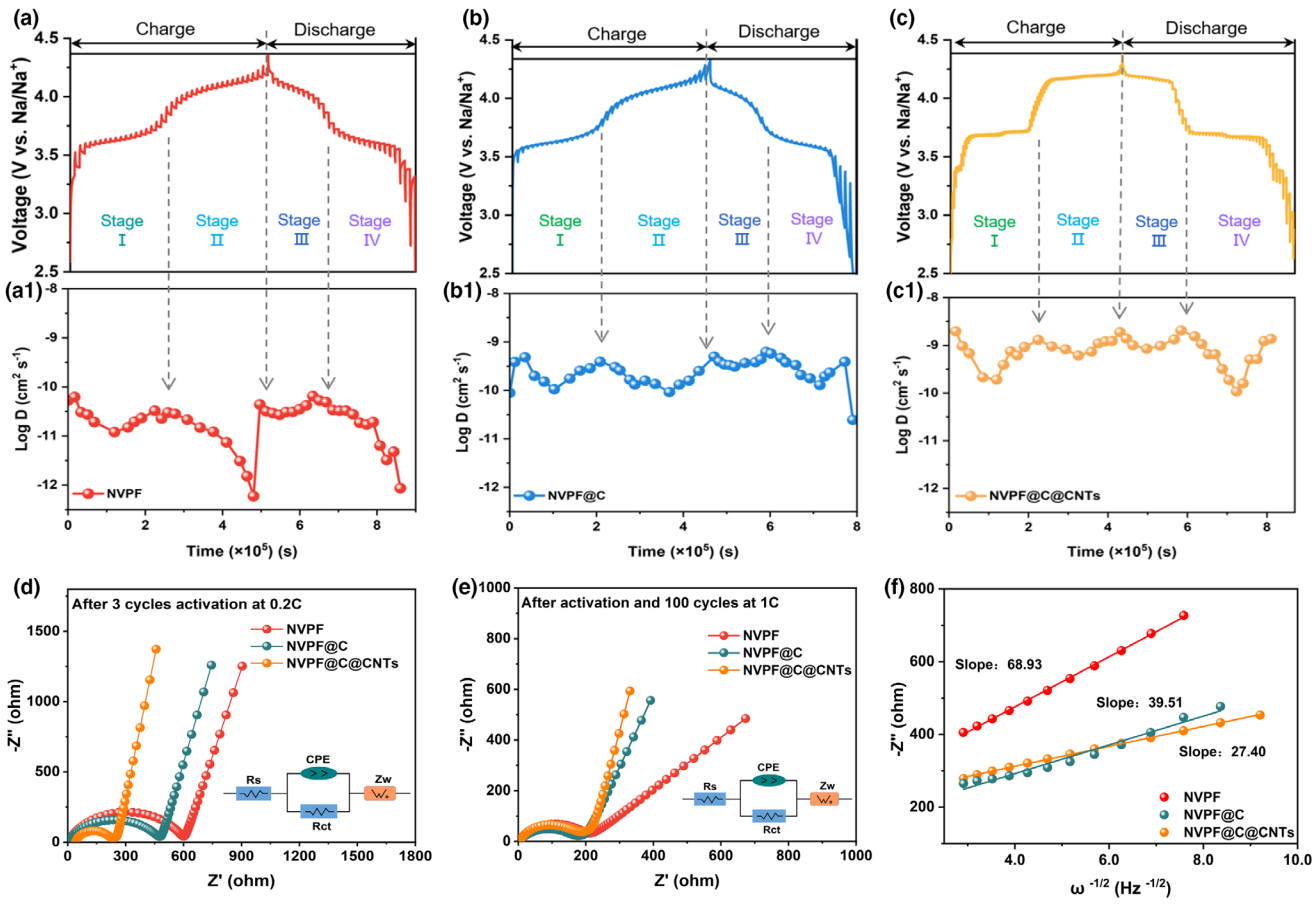

Figure 7. Na-migration kinetic properties for all NVPF-based materials in half-cells. a–c1) GITT profiles and Na^+ diffusion coefficient of all samples at different charge/discharge states. d, e) Nyquist plots of all samples after activation and after 100 cycles at 1 C, insets are corresponding fitted equivalent circuits and corresponding results display in Table S7. f) The relationship between Z′ and $\omega^{-1/2}$ after 100 cycles at 1 C.

© 2022 The Authors. *Energy & Environmental Materials* published by John Wiley & Sons Australia, Ltd on behalf of Zhengzhou University.

25750356, 0, Downloaded from https://onlinelibrary.wiley.com/doi/10.1002/eem2.12485 by Manchester Metropolitan University, Wiley Online Library on [23/06/2023]. See the Terms and Conditions (https://onlinelibrary.wiley.com/terms-and-conditions) on Wiley Online Library for rules of use; OA articles are governed by the applicable Creative Commons License

passivation film capacitance.[29] The obtained impedance parameters are listed in Table S7, Supporting Information. Notably, the NVPF@C@CNTs electrode after activation demonstrates a much lower Rct (201.7 Ω) compared with those of NVPF (592.1 Ω) and NVPF@C (470.5 Ω), which is beneficial for decreasing the kinetics restriction. Additionally, all the Rct values are decreased after 100 cycles, as the electrode surface is activated through the charging/discharging process. Besides, the relationship between the real part of the impedance at low frequencies for sample after 100 cycles is compared (Figure 7f). The smaller slope values mean faster sodium-ion diffusion in the electrochemical processes, proving that the introduction of coating carbon and CNTs can boost sodium migration of NVPF particles, which further confirms this unique cross-linked dual-carbon networks could enhance the rate performances of the samples.

2.4. Electrochemical Performances of Sodium-Ion Full Cell

To evaluate the feasibility of NVPF@C@CNTs electrode in potential practical application, full cells were assembled by using the NVPF@C@CNTs as cathode and hard carbon (HC) as anode[30,31] (**Figure 8**a). Before the full cells assembling, HC anodes were chemically pre-sodiated at 30 mA g^{-1} to reduce the irreversibility and enhance the stability of the full cell during cycling.[32] Figure 8b shows the charge/discharge curves of NVPF@C@CNTs cathode and HC anode in half cells, respectively. Owing to the low sodiation/desodiation potentials of HC anode, the GCD tests of full cells show smooth charge/discharge profiles (Figure 8c), which is in good agreement with those of NVPF@C@CNTs half cells. Under the current density of 0.1 C between 4.3 and 2.0 V, this full cell exhibits an initial discharge capacity of 120.8 mAh g^{-1}, with a high energy density of 405.5 Wh kg^{-1} (based on the cathode mass) (Figure 8d). Satisfactory reversible capacities of 120.8, 117, 113.6, 111.3, 105.7 and 97.8 mAh g^{-1} are reached at rates of 0.1, 0.5, 1, 2, 5 and 10 C, respectively. Figure 8e shows the application of NVPF@C@CNTs//HC SIBs, where over 1.1 kg NVPF@C@CNTs composites were synthesized through the method described in the experimental part, indicating the advantages in rapid mass preparation of active material. Interestingly, a coin-type full cell (NVPF@C@CNTs//HC) can power the electronic scale. After 100 cycles under 1 C at room temperature, the capacity retention is about 91.5%, (Figure 8f) which is slightly lower than NVPF@C@CNTs half battery (Figure 5c) due to the degradation of

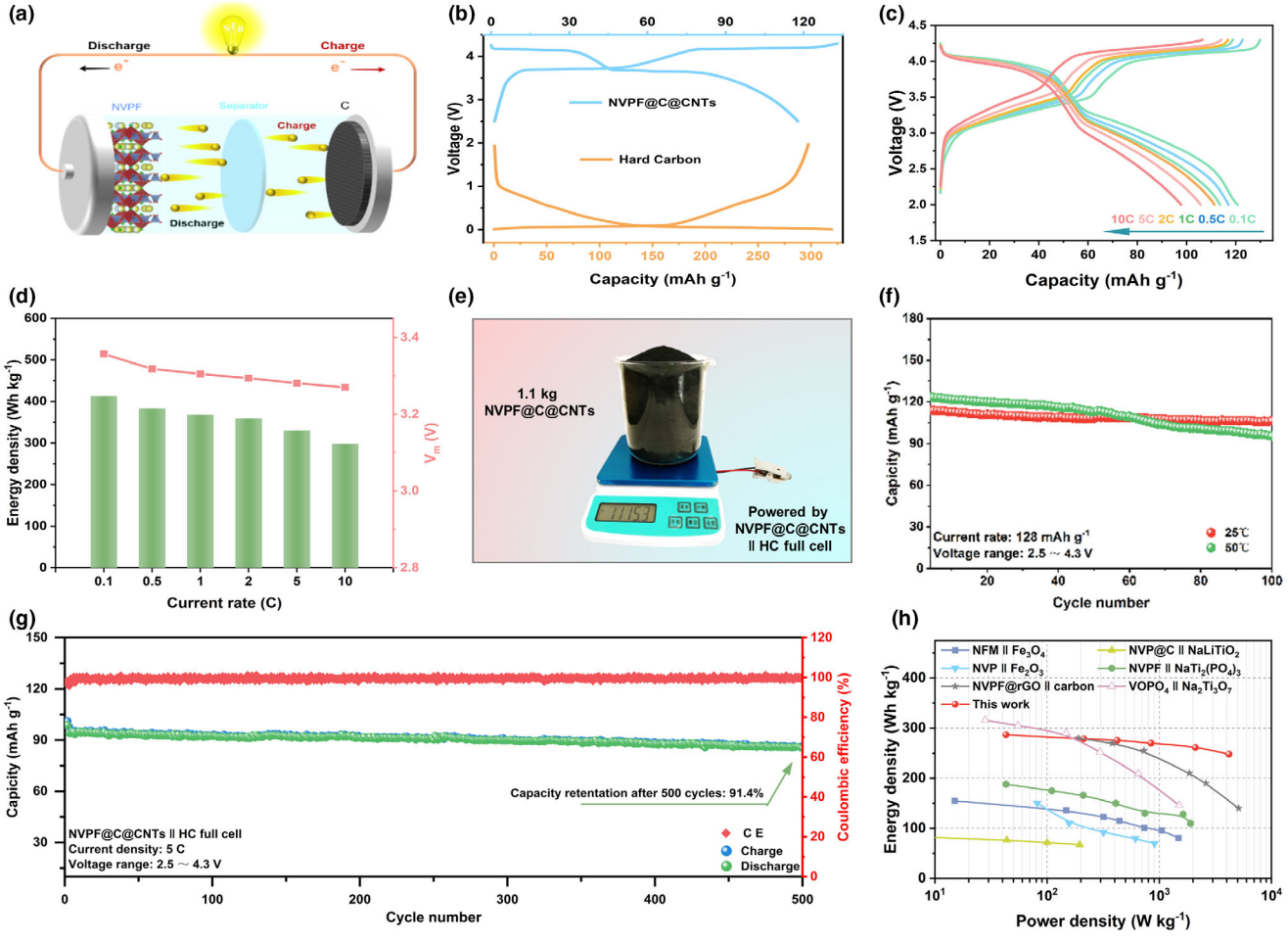

Figure 8. Electrochemical performances of NVPF@C@CNTs//HC full cells. a) Schematic of full SIB of NVPF@C@CNTs//HC. b) GCD curves of NVPF@C@CNTs and hard carbon anode. c) Rate capabilities of full cell from 0.1 C to 10 C and d) corresponding mid-working discharge voltage and energy density. e) Photograph of NVPF@C@CNTs and electronic scale power by the coin full cell. f) Cycling performances at 1 C at different temperature. g) Long-term cycling performances at 5 C for 500 cycles and h) the Ragone plots.

© 2022 The Authors. *Energy & Environmental Materials* published by John Wiley & Sons Australia, Ltd on behalf of Zhengzhou University.

25750356, 0, Downloaded from https://onlinelibrary.wiley.com/doi/10.1002/eem2.12485 by Manchester Metropolitan University, Wiley Online Library on [23/06/2023]. See the Terms and Conditions (https://onlinelibrary.wiley.com/terms-and-conditions) on Wiley Online Library for rules of use; OA articles are governed by the applicable Creative Commons License

hard carbon anode. In addition, the performances of full cells were investigated under extreme temperature conditions. The cell exhibits a higher initial discharge capacity (122.9 mAh g^{-1}) at 50 °C than that at room temperature (115.9 mAh g^{-1}) due to the increased activity of sodium ion. Moreover, long-term stability of the full cell was investigated as well. The specific capacity of NVPF@C@CNTs//HC SIB is about 91.4% left after 500 cycles with an initial discharge capacity of 98.9 mAh g^{-1} at 5 C, demonstrating excellent cycling performances (Figure 8g). Moreover, Ragone plots of this work and other phosphate-based full batteries are given in Figure 8h.[33–40] This NVPF@C@CNTs//HC full cell exhibits an energy density of 278.7 Wh kg^{-1} and a power density of 212.4 W kg^{-1} (based on the total mass of anode and cathode materials). Notably, as the power density reaches 4185.6 W kg^{-1}, a high energy density of 247.9 Wh kg^{-1} can be still left, showing its high potential for practical application.

3. Conclusion

In summary, robust NVPF caged in 3D cross-linked carbon networks composed of carbon layer and intertwined CNTs have been successfully designed and synthesized as cathode materials for full sodium-ion batteries. The NVPF are downsized to ~100 nm because of the introduction of carbonaceous materials, which are functioned as confined microspace. In addition, charge transfer between NVPF@C@CNTs particles is significantly improved due to the increased charge transmission kinetics and shortened ionic transfer pathway. As a consequence, the NVPF@C@CNTs cathode exhibits impressive electrochemical performances, including an initial specific capacity of 126.9 mAh g^{-1} and excellent cycling stability (93.9% capacity retention over 1000 cycles at 20 C). Besides, the NVPF@C@CNTs//HC full batteries reach an energy density of 405.5 Wh kg^{-1} (based on the cathode mass) as well as excellent cycling performances at high temperature (50 °C). It is worth mentioning that 1.1 kg NVPF@C@CNTs composites have been successfully prepared via a solid-state reaction technique, suggesting its huge advantage on mass preparation and commercial application. This enhanced strategy paves a way to accelerate commercial application of SIBs electrode materials.

4. Experimental Section

Detailed information related to the synthesis of active electrodes, physicochemical characterization, and electrochemical evaluation of bifunctional electrodes towards UOR and supercapacitor application is provided in Supporting Information.

Acknowledgements

This work was financially supported by Science and Technology Foundation of Guizhou Province (QKHZC[2020]2Y037), the Science and Technology Innovation Program of Hunan Province (2020RC4005,2019RS1004), Research start-up funding from Central South University (202044019), Innovation Mover Program of Central South University (2020CX007), National Natural Science Foundation of China (U21A20284). Moreover, the authors thank the U19 station in the National Synchrotron Radiation Laboratory (NSRL) for sXAS measurements and the Shiyanjia Lab (www.shiyanjia.com) for the XPS and TEM characterizations.

Conflict of interest

The authors declare that they have no known competing financial interests or personal relationships that could have appeared to influence the work reported in this paper.

Supporting Information

Supporting Information is available from the Wiley Online Library or from the author.

Keywords

dual-nanocarbon networks, full sodium-ion battery, ion transfer kinetics, $Na_3V_2(PO_4)_2F_3$, NASICON structure

Received: May 19, 2022
Revised: July 1, 2022
Published online: July 11, 2022

[1] H. Song, K. Eom, *Adv. Funct. Mater.* **2020**, *30*, 2003086.
[2] Q. Li, Z. Liu, F. Zheng, R. Liu, J. Lee, G. Xu, G. Zhong, X. Hou, R. Fu, Z. Chen, K. Amine, J. Mi, S. Wu, C. Grey, Y. Yang, *Angew. Chem. Int. Ed.* **2018**, *57*, 11918.
[3] Y. You, A. Manthiram, *Adv Energy Mater* **2017**, *8*, 1701785.
[4] Z. Guo, Y. Zhao, Y. Ding, X. Dong, L. Chen, J. Cao, C. Wang, Y. Xia, H. Peng, Y. Wang, *Chem* **2017**, *3*, 348.
[5] Y. Fang, L. Xiao, X. Ai, Y. Cao, H. Yang, *Adv. Mater.* **2015**, *27*, 5895.
[6] X. Rui, W. Sun, C. Wu, Y. Yu, Q. Yan, *Adv. Mater.* **2015**, *27*, 6670.
[7] P. Wang, Y. You, Y. Yin, Y. Wang, L. Wan, L. Gu, Y. Guo, *Angew. Chem. Int. Ed.* **2016**, *55*, 7445.
[8] Y. Xiao, P. Wang, Y. Yin, Y. Zhu, Y. Niu, X. Zhang, J. Zhang, X. Yu, X. Guo, B. Zhong, Y. Guo, *Adv. Mater.* **2018**, *30*, 1803765.
[9] S. Chen, C. Wu, L. Shen, C. Zhu, Y. Huang, K. Xi, J. Maier, Y. Yu, *Adv. Mater.* **2017**, *29*, 1700431.
[10] Z. Jian, Y. Hu, X. Ji, W. Chen, *Adv. Mater.* **2017**, *29*, 1601925.
[11] R. Rajagopalan, B. Chen, Z. Zhang, X. Wu, Y. Du, Y. Huang, B. Li, Y. Zong, J. Wang, G. Nam, M. Sindoro, S. Dou, H. Liu, H. Zhang, *Adv. Mater.* **2017**, *29*, 1605694.
[12] J. Guo, P. Wang, X. L. Wu, X. Zhang, Q. Yan, H. Chen, J. Zhang, Y. Guo, *Adv. Mater.* **2017**, *29*, 1701968.
[13] B. Zhang, R. Dugas, G. Rousse, P. Rozier, A. Abakumov, J. Tarascon, *Nat. Commun.* **2016**, *7*, 10308.
[14] G. Yan, S. Mariyappan, G. Rousse, Q. Jacquet, M. Deschamps, R. David, B. Mirvaux, J. W. Freeland, J. M. Tarascon, *Nat. Commun.* **2019**, *10*, 585.
[15] F. Li, Y. F. Zhao, L. S. Xia, Z. D. Yang, J. P. Wei, Z. Zhou, *J. Mater. Chem. A* **2020**, *8*, 12931.
[16] M. Peng, B. Li, H. Yan, D. Zhang, X. Wang, D. Xia, G. Guo, *Angew. Chem. Int. Ed.* **2015**, *54*, 6452.
[17] Y. Qi, Z. Tong, J. Zhao, L. Ma, T. Wu, H. Liu, C. Yang, J. Lu, Y.-S. Hu, *Joule* **2018**, *2*, 2348.
[18] F. Li, Z. Zhou, *Small* **2018**, *14*, 1702961.
[19] C. Zhu, P. Kopold, P. van Aken, J. Maier, Y. Yu, *Adv. Mater.* **2016**, *28*, 2409.
[20] M. Chen, L. Chen, Z. Hu, Q. Liu, B. Zhang, Y. Hu, Q. Gu, J. Wang, L. Wang, X. Guo, S. Chou, S. Dou, *Adv. Mater.* **2017**, *29*, 1605535.
[21] H. Hou, C. Banks, M. Jing, Y. Zhang, X. Ji, *Adv. Mater.* **2015**, *27*, 7861.
[22] Q. Liu, D. Wang, X. Yang, N. Chen, C. Wang, X. Bie, Y. Wei, G. Chen, F. Du, *J. Mater. Chem. A* **2015**, *3*, 21478.
[23] Y. Zhang, T. Wang, Y. K. Tang, Y. D. Huang, D. Z. Jia, Y. Guo, Z. Zhou, *J. Power Sources* **2021**, *516*, 230515.
[24] W. Shen, H. Li, Z. Guo, C. Wang, Z. Li, Q. Xu, H. Liu, Y. Wang, Y. Xia, *ACS Appl. Mater. Interfaces* **2016**, *8*, 15341.
[25] W. Song, X. Cao, Z. Wu, J. Chen, Y. Zhu, H. Hou, Q. Lan, X. Ji, *Langmuir* **2014**, *30*, 12438.
[26] W. Song, X. Ji, Z. Wu, Y. Yang, Z. Zhou, F. Li, Q. Chen, C. E. Banks, *J. Power Sources* **2014**, *256*, 258.

© 2022 The Authors. *Energy & Environmental Materials* published by John Wiley & Sons Australia, Ltd on behalf of Zhengzhou University.

25750356, 0, Downloaded from https://onlinelibrary.wiley.com/doi/10.1002/eem2.12485 by Manchester Metropolitan University, Wiley Online Library on [23/06/2023]. See the Terms and Conditions (https://onlinelibrary.wiley.com/terms-and-conditions) on Wiley Online Library for rules of use; OA articles are governed by the applicable Creative Commons License

[27] J. Hou, M. Hadouchi, L. Sui, J. Liu, M. Tang, W. Kan, M. Avdeev, G. Zhong, Y. Liao, Y. Lai, Y. Chu, H. Lin, C. Chen, Z. Hu, Y. Huang, J. Ma, *Energy Stor. Mater.* **2021**, *42*, 307.
[28] G. Cui, Q. Dong, Z. Wang, X. Liao, S. Yuan, M. Jiang, Y. Shen, H. Wang, H. Che, Y. He, Z. Ma, *Nano Energy* **2021**, *89*, 106003.
[29] K. Zhang, X. Zhang, W. He, W. Xu, G. Xu, X. Yi, X. Yang, J. Zhu, *J. Mater. Chem. A* **2019**, *7*, 9890.
[30] B. Hou, Y. Wang, Q. Ning, W. Li, X. Xi, X. Yang, H. Liang, X. Feng, X. Wu, *Adv. Mater.* **2019**, *31*, 1903125.
[31] Z. Li, Z. Jian, X. Wang, I. Rodriguez, C. Bommier, X. Ji, *Chem. Commun. (Camb.)* **2017**, *53*, 2610.
[32] X. Shen, Q. Zhou, M. Han, X. Qi, B. Li, Q. Zhang, J. Zhao, C. Yang, H. Liu, Y. Hu, *Nat. Commun.* **2021**, *12*, 2848.
[33] S. Oh, S. Myung, C. Yoon, J. Lu, J. Hassoun, B. Scrosati, K. Amine, Y. Sun, *Nano Lett.* **2014**, *14*, 1620.
[34] M. Lopez, M. Aragon, G. Ortiz, P. Lavela, R. Alcantara, J. Tirado, *Chemistry* **2015**, *21*, 14879.
[35] Y. Sun, L. Zhao, H. Pan, X. Lu, L. Gu, Y. Hu, H. Li, M. Armand, Y. Ikuhara, L. Chen, X. Huang, *Nat. Commun.* **2013**, *4*, 1870.
[36] Y. Fang, L. Xiao, J. Qian, Y. Cao, X. Ai, Y. Huang, H. Yang, *Adv. Energy Mater.* **2016**, *6*, 1502197.
[37] Y. Cai, X. Cao, Z. Luo, G. Fang, F. Liu, J. Zhou, A. Pan, S. Liang, *Adv. Sci.* **2018**, *5*, 1800680.
[38] W. Ren, Z. Zheng, C. Xu, C. Niu, Q. Wei, Q. An, K. Zhao, M. Yan, M. Qin, L. Mai, *Nano Energy* **2016**, *25*, 145.
[39] C. Yang, X. Ji, X. Fan, T. Gao, L. Suo, F. Wang, W. Sun, J. Chen, L. Chen, F. Han, L. Miao, K. Xu, K. Gerasopoulos, C. Wang, *Adv. Mater.* **2017**, *29*, 1701972.
[40] L. Dong, L. Chen, X. Su, Y. Wang, Y. Xia, *Angew. Chem. Int. Ed.* **2016**, *55*, 7474.

© 2022 The Authors. *Energy & Environmental Materials* published by John Wiley & Sons Australia, Ltd on behalf of Zhengzhou University.

25750356, 0, Downloaded from https://onlinelibrary.wiley.com/doi/10.1002/eem2.12485 by Manchester Metropolitan University, Wiley Online Library on [23/06/2023]. See the Terms and Conditions (https://onlinelibrary.wiley.com/terms-and-conditions) on Wiley Online Library for rules of use; OA articles are governed by the applicable Creative Commons License